A numerical study of Lamb wave localisation in thin plates using a passive co-linear phased array

Luke Pollock[1]* & Graham Wild[2]

[1]School of Engineering and Technology, UNSW Canberra, ACT, 2612, Australia

[2]School of Science, UNSW Canberra, ACT, 2612, Australia

Abstract

Lamb waves have become increasingly popular in the field of aerospace vehicle non-destructive testing and evaluation as well as structural health monitoring. These guided waves possess the ability to travel long distances and exhibit a notable inclination to interact with existing damage. This work has numerically explored the use of a passive co-linear phased array to localise emission sources over a wide range of variables. Three localisation methods are explored, namely, reverse beamforming, wavefront curvature ranging, and hyperbolic lateration. It was shown that both reverse beamforming and wavefront curvature ranging could localise an emission with <1% error in both range and bearing, while hyperbolic lateration was significantly worse. A relationship between bearing error and bearing was demonstrated, presenting the ability to develop new methods with correction factors that can localise emissions with even greater accuracy.

* Corresponding Author

L.POLLOCK@ADFA.EDU.AU

1. Introduction

This paper explores several methods for the passive localisation of Lamb waves in thin plate-like structures. Lamb waves are a form of non-linear, elastic, guided wave that propagate in thin plate-like structures [1]. The ability to localise Lamb waves is a powerful method for the structural health monitoring (SHM) of an aerospace vehicle such that the damage can be interrogated further or flagged for inspection at a regular maintenance interval. The nature of Lamb wave propagation is such that the behaviour is dispersive, i.e., each frequency travels at a different velocity. The presence of dispersion within Lamb waves makes their analysis difficult with traditional methods. Several techniques have been proposed for the removal of dispersion using post-processing analysis, however, few methods have been proposed in which the sensor configuration is optimised for the minimisation of dispersion [2]. As such, this paper proposes a technique that utilises the close spacing of a phased array style sensor array such that the dispersion of the Lamb wave signal may be considered negligible. The ability to make this assumption provides new opportunities for the localisation of AEs with this type of sensor array. The array could also be used for the analysis of other forms of acoustic emissions such as Rayleigh, Love and shear waves [3].

1.1. Structural Health Monitoring

SHM for aerospace vehicles is an invaluable tool in maintaining the integrity and health of a structure. With many similarities to non-destructive testing and evaluation (NDT&E), SHM operates in-situ, providing real-time information about the health of a structure to render damage assessments and provide prognostics [4-6]. The environment in which aerospace vehicles operate and the increasing demand for lighter structures to meet emissions targets and reduce costs motivate the development of an SHM network [7]. Such a network can provide real-time information regarding the health of the vehicle to allow for improved decision making and to aid in the development of condition-based maintenance schedules. Additional benefits from the sensor networks required for SHM include the ability to inform digital twin models and power an Industry 4.0 movement that could rapidly decrease vehicle down-time as well as improving safety [8]. The information collected can also contribute to powering future data-driven design innovations.

Bartelds [9] explored the applications of a piezoelectric transducer (PZT) network for inspection, reflecting upon how the inspection process remained the weakest link in the reliability chain. [9] found that such a network could reduce inspection time by up to 50% for military aircraft and that total maintenance and inspection costs could be reduced by up to 20% for the civil sector. Dong and Kim [10] completed a cost-benefit analysis of a SHM network for fuselage structures in civil aviation aircraft and found that despite inspection and maintenance amounting for more than 27% of the overall life cycle costs of aircraft, such a network would not be cost effective with current technology limitations [11]. Dong concluded that more work should be performed to develop methods that would decrease the number of sensors required for monitoring. The proposed passive phased array (PPA) sensor configuration in this work presents as a useful method for the monitoring of large areas with a relatively small array, requiring few sensors.

With an estimated 55% of aircraft structural failures accredited to some form of fatigue damage, fatigue remains a persistent problem for the aviation industry [12]. Moreover, uncertainty in the loading and environmental conditions that the vehicle is exposed to can render design work inadequate for the application. Goranson [13] showed that differences between operating stresses and fatigue allowables resulted in up to 85% of service problems for long-life structures.

Moreover, the increasing use of composite materials in aerospace structures, whilst presenting new opportunities, also presents with new challenges that must be overcome [4, 14-16]. Fibre composites, whilst typically less affected from fatigue than metals, introduce new damage modes such as delamination, matrix cracking, fibre pull-out and fibre breakage, requiring new methods for monitoring [17].

Furthermore, recent work has revealed the growing issue of fatigue damage in propulsion systems [18], unveiling the importance of future work into not just the health of the structure but that of the entire vehicle with the implementation of an integrated vehicular health management (IVHM) system. Ultimately, the development of new methods for the NDT&E and SHM of aerospace structures and systems is important for improving the safety and performance of aerospace vehicles.

1.2. Lamb Waves

The theory of Lamb waves originates from the work of Horace Lamb in 1917 [1]. By applying a Helmholtz decomposition to the elastodynamic constitutive equation for isotropic and homogenous materials with a traction free boundary condition, Lamb derived the governing equation for the behaviour of such waves [1, 3]. These governing equations, known as the Rayleigh-Lamb equations, revealed that Lamb waves are composed of two modes: symmetric and antisymmetric. An infinite number of modes can exist in a plate simultaneously [19]. The Rayleigh-Lamb equations are shown below for both modes and indicates that the behaviour of the waves is non-linear and dispersive within the medium.

$$\frac{\tan(qh)}{\tan(ph)} = -\frac{4k^2qh}{(k^2-q^2)^{\ 2}} \tag{1.1}$$

$$\frac{\tan(qh)}{\tan(ph)} = -\frac{(k^2-q^2)^{\ 2}}{4k^2qh} \tag{1.2}$$

These equations can be solved by applying a variety of numerical schemes. The depiction of the resulting solution is often given in the form of dispersion curves for a particular material and frequency-thickness product. An example of such a curve is shown in Figure 1.

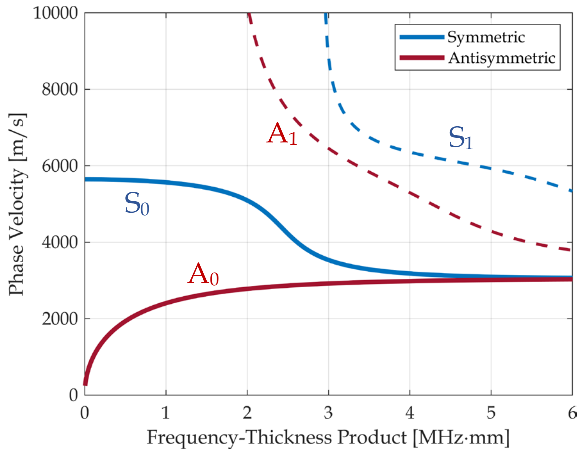

Figure 1: Lamb wave dispersion curves for an aluminium plate [19].

As is evident from the dispersion curve, the presence of higher order modes only exists above a certain frequency-thickness product, often known as the cut-off frequency. The restriction of analysis to only the fundamental, or zeroth order, wave modes simplifies their analysis greatly and is often applied in literature [20-22]. Whilst the fundamental order modes are the most studied, the analysis of higher order modes, although difficult, can provide useful information regarding the health of the structure [23, 24].

1.3. Phased Arrays

A phased array is a form of steered sensor array in which a phase delay between adjacent sensors can steer the direction of a wavefront [25, 26]. Phased arrays have been extensively used in radar technology because of their simplicity and absence of moving parts. While they are commonly used for steering electromagnetic wavefronts, phased arrays have also found applications in acoustics, such as sonography (biomedical imaging), seismology (oil and gas prospecting), and sonar. Phased arrays have also been applied in the fields of NDT&E and SHM for the steering of ultrasonic waves to scan a material for damage or to interrogate a specific location [4, 27-29]. The use of such an array allows for monitoring a large area with a relatively small sensor array. In all of these applications, the phased array is actively employed, in which the array is being used to generate the wavefront. The use of active sensing is generally employed with time of arrival (ToA) algorithms that can localise and interrogate a defect based upon the time required for the wave to return to the array [30].

As an alternative, this work has explored the use of phased arrays in a passive sense, in which the array passively collects AE information from the structure for interrogation. In this manner, ToA algorithms cannot be applied as the time that the signal was generated is unknown. Passive phased arrays rely on the measurement of time difference of arrival (TDoA), which determines the time difference between the reception of the signal by adjacent sensors. The use of TDoA can be applied to a variety of methods for the localisation of an emission. A minimum of three sensors is required for any such method to localise an acoustic source on a two-dimensional plane. An additional benefit of using a PPA is the availability of sensors for detecting emissions. The most common sensor used in active phased array monitoring is that of PZT, that can function as both actuators, for generating the wavefront, and sensors, for acquiring the returned signal. By eliminating the need to generate a signal, alternative sensors such as fibre Bragg gratings (FBGs), fibre lasers, or laser Doppler vibrometers (LDVs) can be employed, each with its own unique merits. Table 1 provides a summary of some passive sensors that can be used in a phased array configuration.

Table 1: A summary of sensors that could be employed for passive phased array localisation.

Sensor	Measurement Type
PZT	Electrical – Piezoelectric effect
Strain Gauge	Electrical - Resistivity
CMUTs	Electrical - Capacitance
FBG	Optical
LDVR	Optical

2. Methodology

2.1. Time Difference of Arrival

In order to calculate the TDoA between adjacent sensors, a variety of methods may be employed. For generalised sparse arrays, the simplest technique is to set a threshold value, either in the time or frequency domain, to determine when a signal is considered 'arrived'. Determining the difference in time between the arrival for all sensors yields the TDoA. Although this method is useful, it is prone to error. The inherent dispersion in the signals causes the arrival point of the signal to change as it travels. Furthermore, the amplitude-dependent approach is highly susceptible to the presence of noise. A more robust method of determining time delay is via the use of the generalised cross correlation (GCC).

2.2. Generalised Cross-Correlation

By employing a phased array style configuration and assuming that the dispersion between adjacent elements is negligible, the GCC between each signal should provide an accurate estimation of the time delay [31-33]. The GCC method operates as a sliding dot product to determine the most probable time lag between two signals [34-36]. GCC is a special variant of the cross-correlation function that is performed in the frequency domain. It is in the frequency domain that the potential for applying a weighting function is presented. Several weighting functions exist, including the phase transform (PhaT), Roth transform (ROTH), and smoothed coherence factor transform (SCOT) [31-33, 37, 38]. The cross-correlation function for a pair of discrete signals in the time domain is shown in Equation 2 where $\overline{x_\imath[k]}$ represents the complex conjugate of signal $x_i[k]$ [34-36].

$$(x_i \star x_j)[n] \triangleq \lim_{N\to\infty} \sum_{k=-N}^{N} \overline{x_\imath[k]} x_j[k+n] \tag{2}$$

For the case that dispersion is assumed as negligible, the signal x_j is assumed to be a scaled, delayed and translated copy of signal x_i, both with varying zero mean noise components.

$$x_i = s_1(t) + n_i(t) \tag{3.1}$$
$$x_j = As_1(t+\tau_{ij}) + n_j(t) \tag{3.2}$$

The cross-correlation function can be more efficiently computed in the frequency domain using the inverse fast Fourier transformation (IFFT) from which the most likely time lag is calculated as follows. Where $X_i(f)$ is the fast Fourier transform (FFT) of signal $x_i[k]$ and $\psi[k]$ is the desired frequency weighting function. For the case of regular cross-correlation, $\psi[k] = 1$.

$$\tau_{ij} = \max \mathbf{IFFT} \left| \psi[k] \cdot \overline{X_\imath[k]} \cdot X_j[k] \right| \tag{4}$$

2.3. Localisation Algorithms

2.3.1. Reverse Beamforming

Reverse beamforming (RB) theory is derived from the principles of time-delay-and-sum beamforming, commonly used for wavefront steering. This work has investigated the application of time-delay-and-sum beamforming in the time domain, although frequency domain methods also exist. Using the TDoA between sensor pair i, j, as given by τ_{ij}, the direction of arrival (DoA) may be determined as follows [6].

$$\theta_{ij} = \arccos\left(\frac{V\tau_{ij}}{L_{ij}}\right) \tag{5}$$

Where V is the velocity of the signal and $L_{ij}$is the distance between the adjacent sensors. The DoA is measured counterclockwise relative to the axis connecting the sensor pair, with reference to their midpoint.

The velocity of the Lamb wave is not constant due to its dispersive nature, as it depends on the frequency. Hence, the selection of velocity is an important parameter and one that is open to uncertainty. In this work, the velocity is determined from the peak frequency component of the signal, identified through the power spectral density (PSD). Often, it is necessary to optimise the velocity selection dependent upon the method in which the time delay is determined. Alternative techniques such as weighted functions and Bayesian inferencing may be useful in increasing the accuracy of the calculated DoA.

Using two sensor pairs (three sensors total), the two calculated DoA values may be used to obtain the estimate of the source. The AE is estimated as the location in which the two DoA values relative to the sensor array intersect. By creating two lines between the sensor pairs, the relative location of the emission for a co-linear sensor array with regular spacing is given below.

$$x_s = \frac{L}{2} \cdot \frac{\tan(\theta_{23}) + \tan(\theta_{12})}{\tan(\theta_{23}) - \tan(\theta_{12})} \tag{6.1}$$

$$y_s = \frac{L}{2} \cdot \tan(\theta_{12}) \cdot \left(1 + \frac{\tan(\theta_{23}) + \tan(\theta_{12})}{\tan(\theta_{23}) - \tan(\theta_{12})}\right) \tag{6.2}$$

2.3.2. Wavefront Curvature Ranging

Wavefront curvature ranging (WCR) is a method used to estimate the location of an emission source by analysing the curvature of the propagating wavefront. [39]. Although WCR has primarily been applied in underwater localisation using hydrophones, it can also be employed for AE detection without any limitations. WCR initially involves calculating the estimated range of the source, which is then used to determine the bearing. This is in contrast to the method of RB which first determines bearing and then range. The equations for WCR with a co-linear, regularly spaced array are given below.

$$R_s = \frac{(V\tau_{12})^2 + (V\tau_{23})^2 - 2L^2}{2V(\tau_{12} - \tau_{23})} \tag{7.1}$$

$$\theta_s = \arccos\left(\frac{L^2 - 2R_s V\tau_{23} - (V\tau_{23})^2}{2R_s L}\right) \tag{7.2}$$

Localisation using WCR can be easily achieved; however, this method in its current form is limited to co-linear arrays. Modifications can be made to the WCR method to develop a recursive algorithm suitable for non-co-linear arrays; however, this aspect has not been explored.

2.3.3. Hyperbolic Lateration

The technique of hyperbolic lateration (HL) originates from the application of multilateration, where the source of an emission can be determined by intersecting two circles based on the Time of Arrival (ToA). This method is extended for TDoA applications in which the intersection of two circles becomes two hyperbolae.

$$V\tau_{ij} = \sqrt{(x_s - x_i)^2 + (y_s - y_i)^2} - \sqrt{(x_s - x_j)^2 + (y_s - y_j)^2} \tag{8}$$

The location of the source can be determined by simultaneously solving the equations of two hyperbolae. Numerical methods are commonly employed to solve these equations due to their non-linearity. Unlike RB and WCR, where the DoA must be determined first and then the source localized, HL is a one-step method where the source is immediately determined from the numerical solution of the simultaneous equations. Similar to RB, HL can be applied to any sensor configuration; however, it may take longer to solve and may be less stable due to the need for a numerical solver.

2.4. Parametric Study

A parametric study has been conducted to evaluate the advantages of the PPA configuration. The Lamb wave propagation has been modelled using the numerical model described in [40]. A generic aluminium alloy is employed as the substrate with a unit thickness, the properties of which are given in Both Lamb modes have been separately studied without the addition of any noise.

Table 2. Table 3 presents the complete list of parameters analysed, and Figure 2 depicts the flowchart of the parametric process. Both Lamb modes have been separately studied without the addition of any noise.

Table 2. Mechanical and physical properties of the generic aluminium alloy.

Young's Modulus	Poisson's Ratio	Density	Thickness
70 GPa	0.33	2780 kg/m^3	1.0 mm

Table 3. A list of all parameters used in the parametric study.

Peak Frequency	Sampling Frequency	Lamb Mode	Sensor Spacing	Bearing	Range
100 kHz	1.00 Msps	A_0	1.0 mm	0.0 deg	50.000 mm
200 kHz	10.0 Msps		4.0 mm	5.0 deg	155.56 mm
		S_0	…	…	…
400 kHz	100 Msps		19 mm	90 deg	1000.0 mm

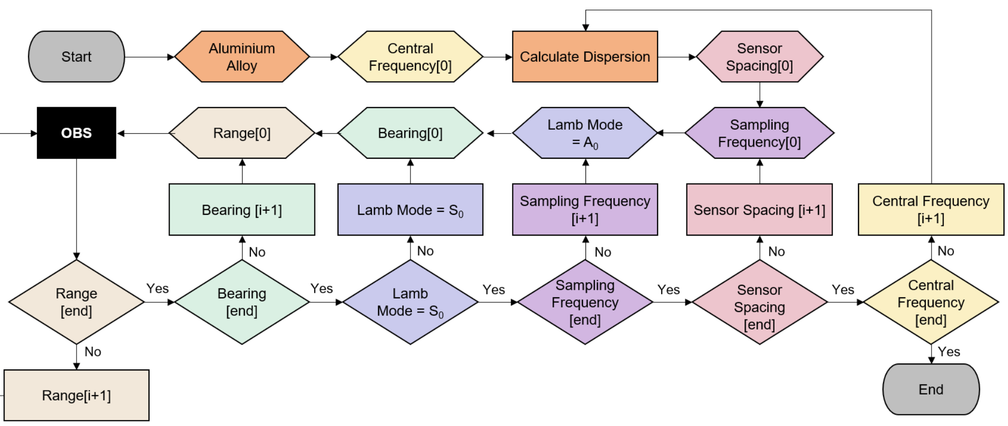

Figure 2. A flow chart of the parametric study process across all assessed variables.

3. Results and Discussion

3.1. Frequency Dependence

The initial set of results pertains to the variation in the peak frequency of the actuating signal. Correspondence is shown here, wherein it is possible for the wavelength of the peak frequency to be less than the sensor spacing. As a consequence, phantom solutions arise, exhibiting mirroring around the 45-degree axis. An example of this is shown in Figure 3.

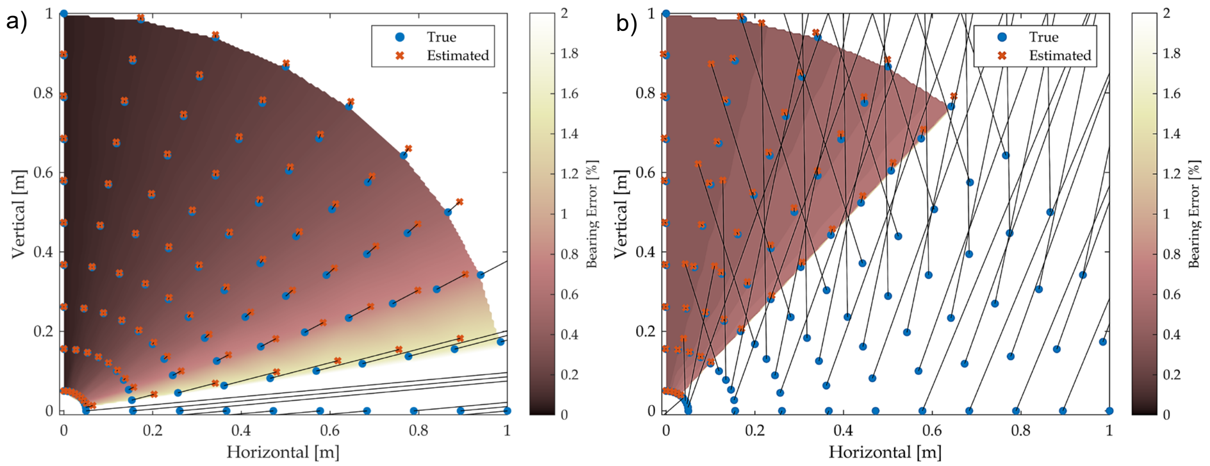

Figure 3. Bearing error maps for a sensor spacing of 7 mm (a) and 10 mm (b) using reverse beamforming. Sampling frequency: 100 Msps. Mode: antisymmetric. Peak frequency: 200 kHz.

To emphasize the sensitivity to this phenomenon, Figure 4 illustrates the average error in range and bearing during the analysis of the antisymmetric mode. The vertical lines in the graph represent the wavelength at each frequency.

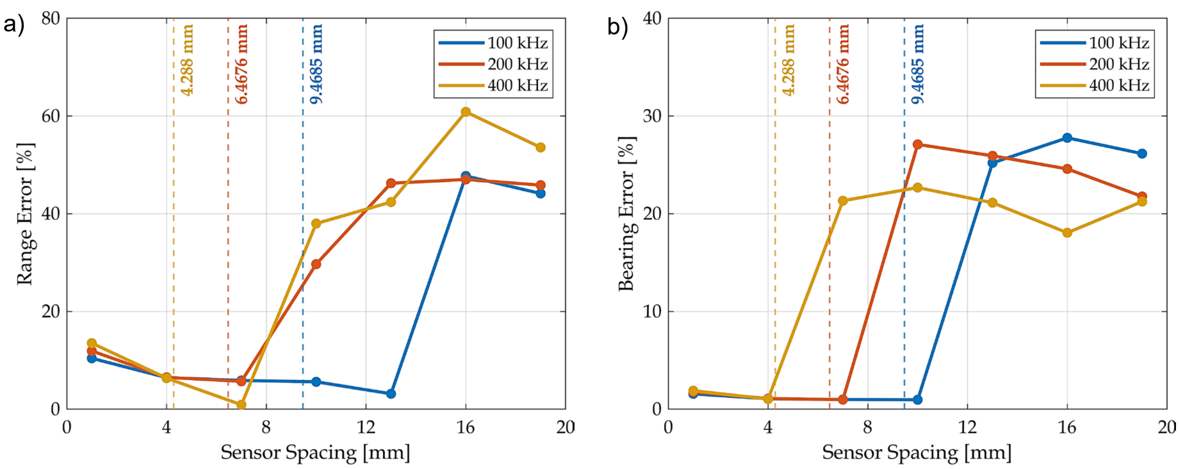

Figure 4. Antisymmetric range (a) and bearing (b) mean error plots as a function of sensor spacing and peak frequencies. Vertical dotted lines indicate the wavelength at the peak frequency.

Figure 5 further exemplifies the effect, revealing that as the peak frequency increases, determining the location of the emission becomes more challenging.

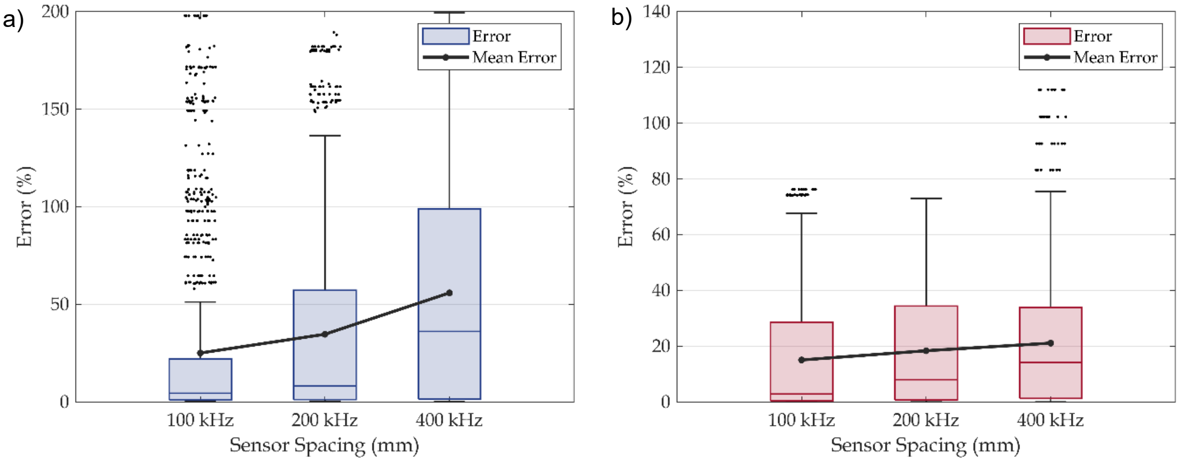

Figure 5. Box plots of range error (a) and bearing error (b) for three peak frequencies. Data includes all sensor spacings, sampling frequencies, and methods, analysing the antisymmetric mode.

An important design consideration for PPAs is the sensor spacing in relation to the peak frequency of the source signal. Figure 6 illustrates the variation of wavelength with frequency for both fundamental modes. Dashed horizontal lines represent wavelengths of 1 mm, 5 mm, and 10 mm, and their intersection with the plots indicates the approximate maximum frequency that can be detected with the corresponding sensor spacings. The summarised data is presented in Table 4. It is noteworthy that higher-order modes necessitate smaller sensor spacings for localising their emissions.

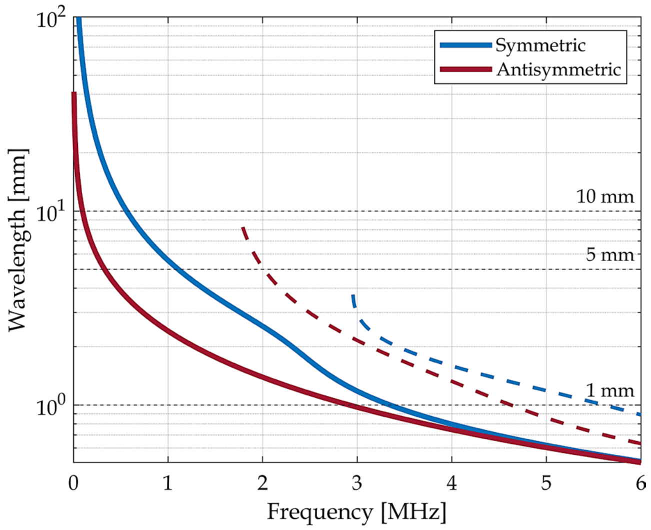

Figure 6. Wavelength as a function of frequency for the symmetric and antisymmetric modes. Horizontal dashed lines indicate wavelengths of 1 mm, 5 mm, and 10 mm.

Table 4. The maximum frequency in which each mode can be analysed for a given sensor spacing.

	1 mm	5 mm	10 mm
S_0 (kHz)	3,345	1,111	564.6
S_1 (kHz)	5,610	NA	NA
A_0 (kHz)	2,913	330.3	96.10
A_1 (kHz)	4,625	2,012	NA

3.2. Sampling Frequency

The subsequent set of analysed results focuses on the effect of sampling frequency. The sampling frequency plays a crucial role in the calculation of cross-correlation between the two signals since the method operates discretely and cannot resolve a time delay smaller than the acquisition period. Figure 7 and Figure 8 illustrate that increasing the sampling frequency leads to a reduction in both ranging and bearing errors.

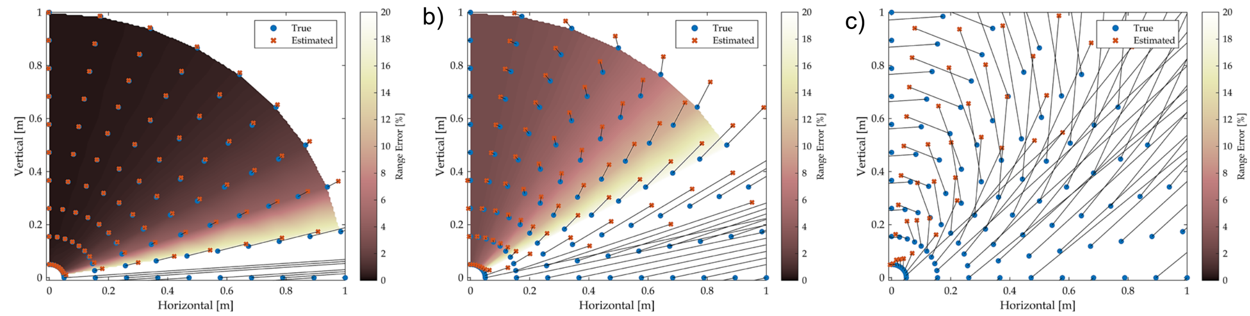

Figure 7. Ranging error maps for a) 100 Msps, b) 10 Msps, and c) 1 Msps. Sensor spacing: 10 mm. Method: reverse beamforming. Peak frequency: 200 kHz. Mode: symmetric.

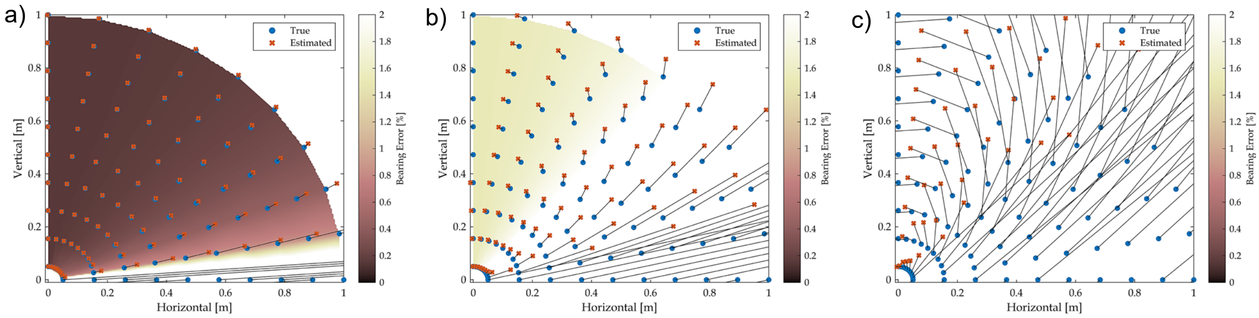

Figure 8. Bearing error maps for a) 100 Msps, b) 10 Msps, and c) 1 Msps. Sensor spacing: 10 mm. Method: reverse beamforming. Peak frequency: 200 kHz. Mode: symmetric.

Figure 9 depicts the relationship between the median error across the physical sampling space. It is evident that the errors are best approximated by a rational function of order (0,1), as shown in Equation 9.

$$f(x) = \frac{p_1}{x + q_1} \tag{9}$$

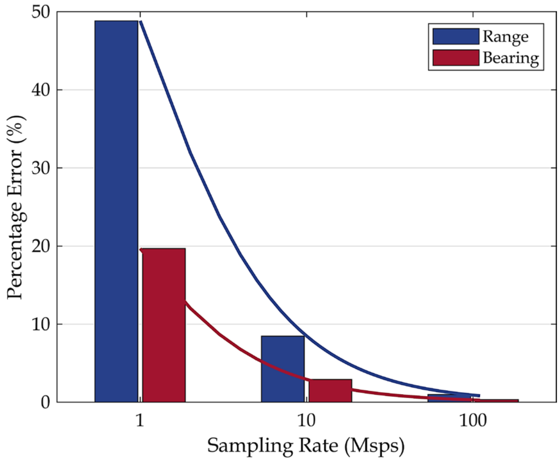

Figure 9. Range and bearing median errors for all sampling frequencies, aggregated across sensor spacings, and analysing the symmetric mode with a peak frequency of 200 kHz. Methods used: reverse beamforming and wavefront curvature ranging. Solid lines represent curve fits using (0,1) order rational functions.

Results are once again shown in Figure 10 where it is evident that all summary statistics decrease with increasing sampling frequency – i.e., errors and uncertainty decrease together.

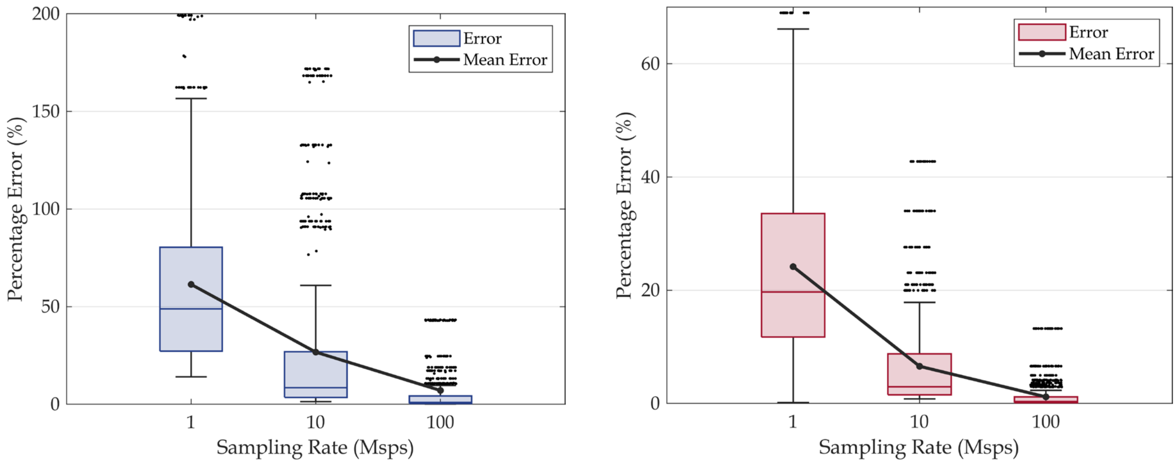

Figure 10. Box plots of range error (a) and bearing error (b) for all sampling frequencies. Data includes all sensor spacings and sampling frequencies, analysing the symmetric mode with a peak frequency of 200 kHz. Methods used: reverse beamforming and wavefront curvature ranging.

3.3. Localisation Methods

After determining the impact of source peak frequency and sampling frequency, a subset of data can be extracted to analyse the localisation methods without bias.. Figure 11 and Figure 12 show error maps for all three assessed methods and range and bearing errors, respectively. It becomes evident that both RB and WCR exhibit similar performance, while the HL method struggles to localise the emission sources. The limited performance of HL is likely due to the numerical method employed to solve the system of equations. A future direction for improvement is to develop a more robust and accurate numerical solver to enhance the localisation performance of HL.

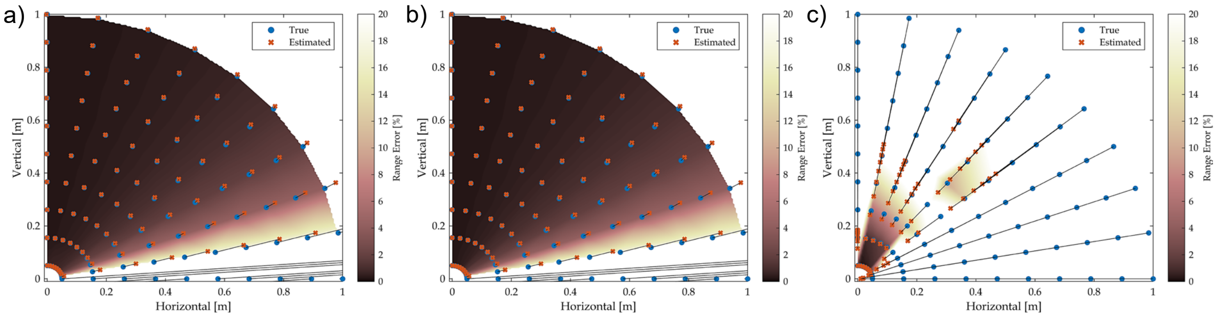

Figure 11. Ranging error maps for a) reverse beamforming, b) wavefront curvature ranging, and c) hyperbolic lateration. Sensor spacing: 10 mm. Sampling frequency: 100 Msps. Peak frequency: 200 kHz. Mode: symmetric.

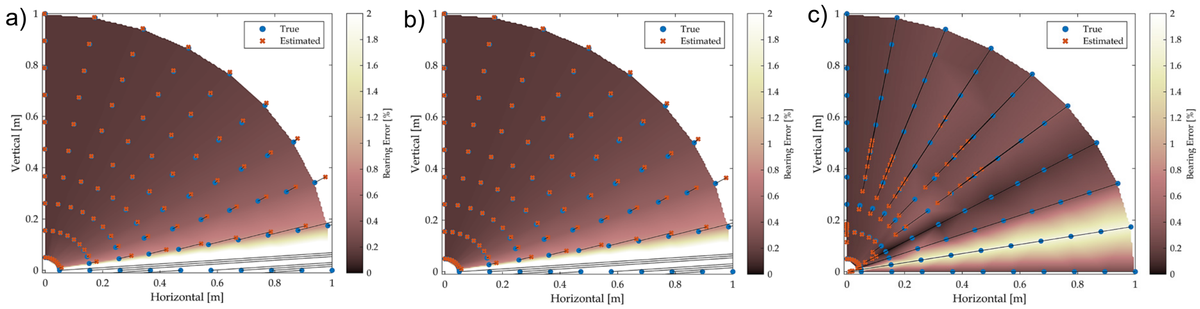

Figure 12. Bearing error maps for a) reverse beamforming, b) wavefront curvature ranging, and c) hyperbolic lateration. Sensor spacing: 10 mm. Sampling frequency: 100 Msps. Peak frequency: 200 kHz. Mode: symmetric.

Median performance is summarised in Figure 13. It is evident that the bearing error for HL is less than that of RB and WCR, however, it is difficult to evaluate if this is in error without improving the algorithm.

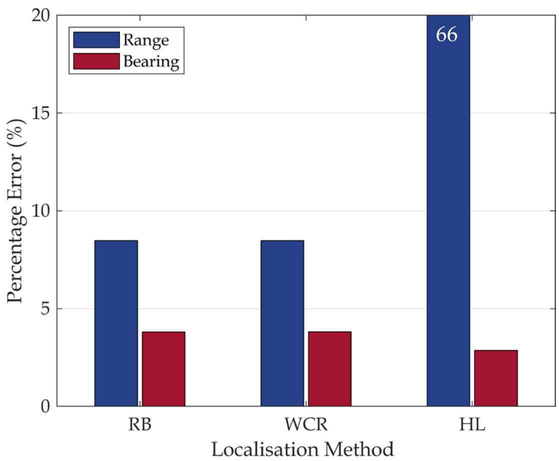

Figure 13. Range and bearing median errors for all localisation methods sampled at 100 Msps, analysing the symmetric mode with a peak frequency of 200 kHz. Data includes all sensor spacings.

Figure 14 presents the summary statistics, indicating that all three methods exhibit similar capabilities in determining the bearing of an emission. However, the HL method shows large ranging errors, as previously discussed. While caution must be exercised when analysing HL results, it is possible that the numerical method has converged on a solution along the source axis. However, further iterations are required to accurately determine the range. Further investigation is planned to address the specific challenges and improve the performance in this area.

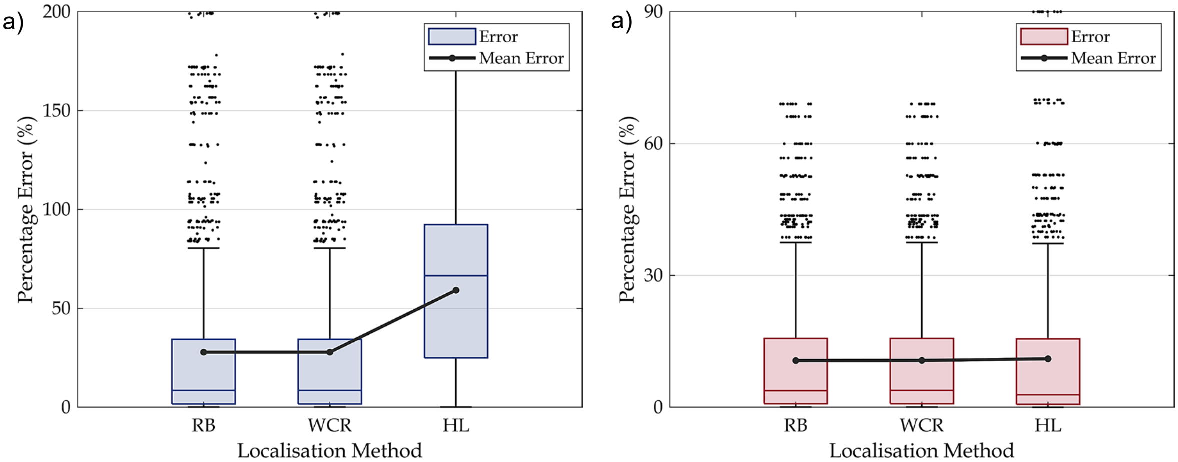

Figure 14. Box plots of range error (a) and bearing error (b) for all localisation methods. Data includes all sensor spacings and sampling frequencies, analysing the symmetric mode with a peak frequency of 200 kHz.

3.4. Sensor Spacing

Building upon the previous discussion, a more comprehensive analysis of the results as a function of sensor spacing is presented in Figure 15 and Figure 16. Once again, a subset of the results is analysed to mitigate bias. The results provide a clear indication that a larger sensor spacing generally improves the resolution of the emission source. This observation contrasts with the requirements for localising higher frequency emissions.

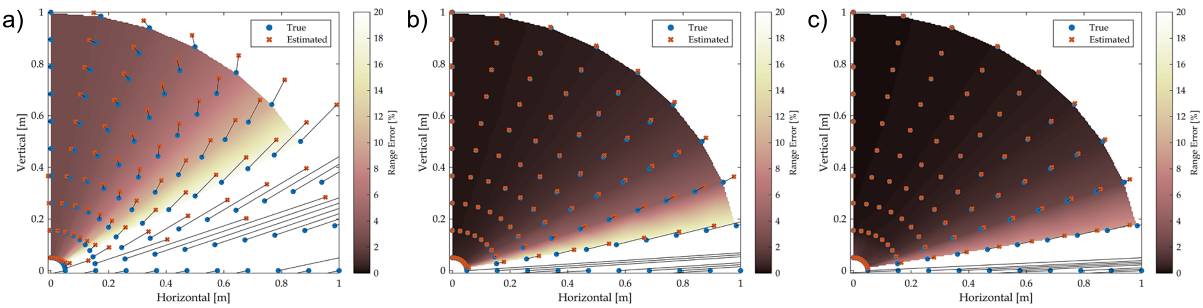

Figure 15. Ranging error maps for sensor spacings of a) 1 mm, b) 10 mm, and c) 19 mm. Data is presented for a sampling frequency of 100 Msps, using the reverse beamforming method, and analysing the symmetric mode with a peak frequency of 200 kHz.

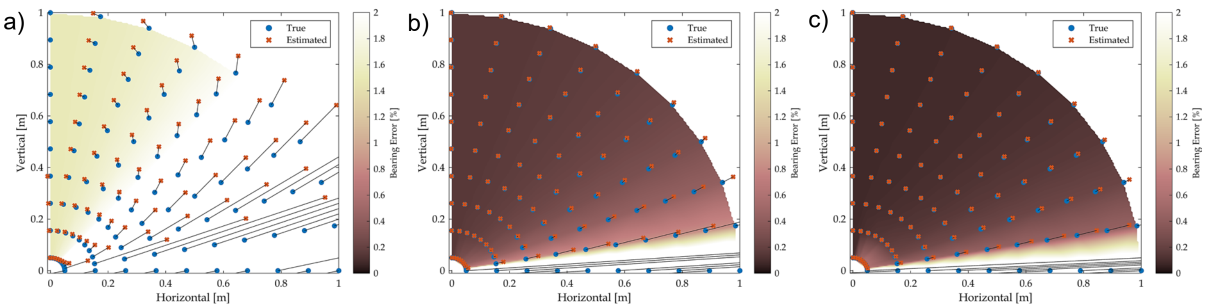

Figure 16. Bearing error maps for sensor spacings of a) 1 mm, b) 10 mm, and c) 19 mm. Data is presented for a sampling frequency of 100 Msps, using the reverse beamforming method, and analysing the symmetric mode with a peak frequency of 200 kHz.

Figure 17 and Figure 18 summarise the error statistics across all sensor spacings. Once again, the median errors are well approximated by a (0,1) order rational function.

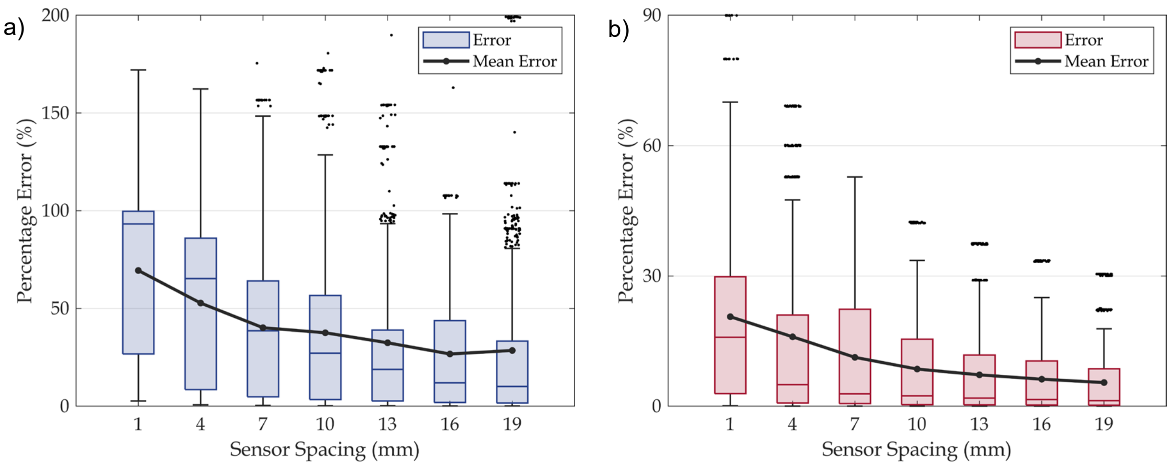

Figure 17. Box plots for a) range error and b) bearing error for all sensor spacings. Data is presented aggregating all sensor spacings, sampling frequencies, and methods, analysing the symmetric mode with a peak frequency of 200 kHz.

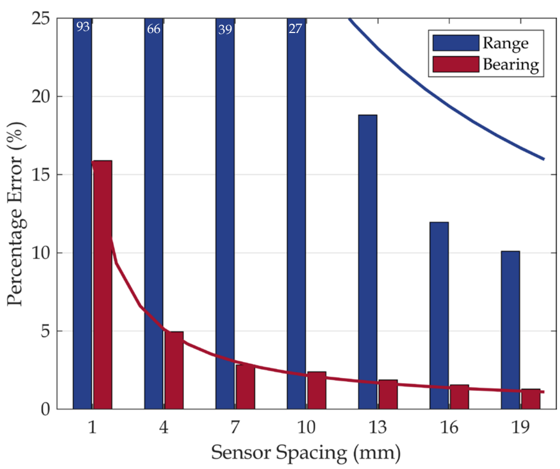

Figure 18. Range and bearing median errors aggregated across all sampling frequencies and sensor spacings, analysing the symmetric mode with a peak frequency of 200 kHz. Solid lines represent curve fits using (0,1) order rational functions.

3.5. Range and Bearing Dependence

The final dataset analysed examines the relationship between error and both the range and direction of the emission. Initial analysis revealed no correlation with range; however, a clear correlation with bearing is evident, as shown in Figure 19. The abrupt changes in error observed with the antisymmetric mode can be attributed to the correspondence phenomenon mentioned earlier. A proposed method, to be explored in future work, involves making corrections based on the bearing to enhance the ability to localise emissions. This method would address the reduced accuracy associated with using an array of small sensor spacings, thus enabling improved localisation of high-frequency emissions.

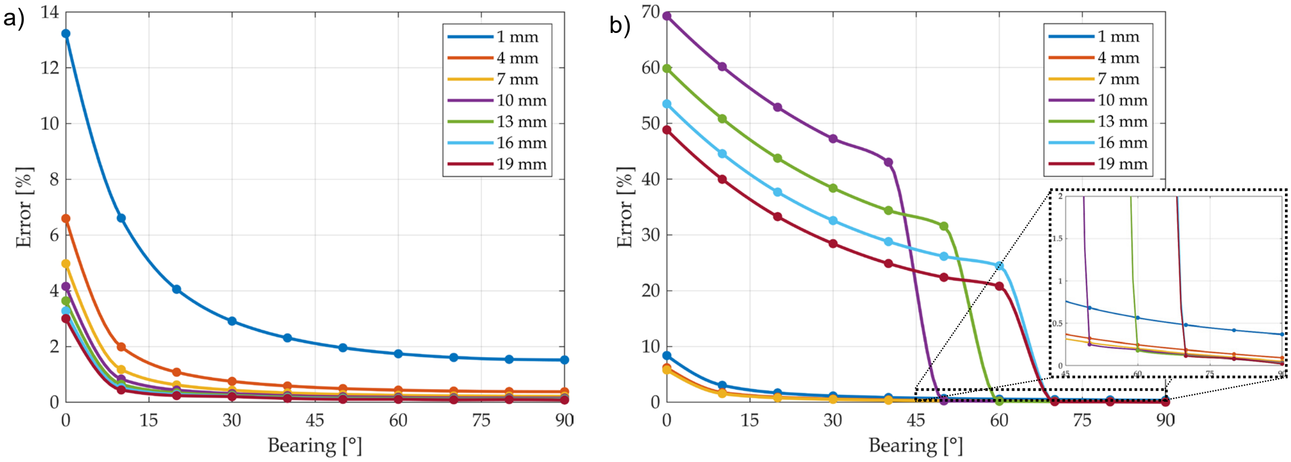

Figure 19. Bearing localisation error for a) the symmetric mode and b) the antisymmetric mode as a function of bearing, with different sensor spacings. Solid lines represent interpolated data using a piecewise cubic Hermite polynomial.

4. Conclusion

In conclusion, this study has investigated the effectiveness of a co-linear passive phased array (PPA) for localising Lamb wave emissions in thin plates. Through a comprehensive parametric study, it has been demonstrated that the PPA can achieve localisation of emissions with an error of less than 1% in both range and bearing. The study examined three localisation methods: reverse beamforming (RB), wavefront curvature ranging (WCR), and hyperbolic lateration (HL).

The results have shown that RB and WCR methods exhibit similar performance, delivering accurate localisation results. However, further improvements are needed for the HL algorithm, as it demonstrated lower accuracy compared to the other methods.

One notable finding is the relationship between the bearing error and bearing, which opens up possibilities for enhancing the localisation methods with correction factors. By incorporating these correction factors, it is anticipated that even greater accuracy in localising emissions can be achieved.

Additionally, the study highlights the importance of sensor spacing in achieving improved localisation accuracy, especially for higher frequency signals. The potential for localising emissions with small sensor spacings paves the way for capturing and analysing higher frequency Lamb waves.

In conclusion, this work contributes to the advancement of Lamb wave localisation techniques using a passive phased array. The findings underscore the viability of RB and WCR methods for non-destructive testing and structural health monitoring applications. Further research is encouraged to refine the HL algorithm and explore the implementation of correction factors for improved localisation accuracy. Ultimately, the study expands our understanding of Lamb wave localisation and its potential for enhancing the assessment of thin plate structures in various industries, particularly in aerospace vehicle non-destructive testing and evaluation, and structural health monitoring.

References

[1] H. Lamb, "On waves in an elastic plate," *Proceedings of the Royal Society of London. Series A, Containing papers of a mathematical and physical character,* vol. 93, no. 648, pp. 114-128, 1917, doi: https://doi.org/10.1098/rspa.1917.0008.

[2] L. Pollock and G. Wild, "Passive Phased Array Acoustic Emission Localisation via Recursive Signal-Averaged Lamb Waves with an Applied Warped Frequency Transformation," 2021, doi: https://doi.org/10.48550/arXiv.2110.06457.

[3] J. L. Rose, *Ultrasonic guided waves in solid media*. Cambridge University Press, 2014.

[4] L. Pollock, S. O'Byrne, and G. Wild, "Quality assurance of uncured polymer matrix prepregs through the application of non-destructive methods," *NDT & E International,* vol. 133, p. 102761, 2023, doi: https://doi.org/10.1016/j.ndteint.2022.102761.

[5] V. Giurgiutiu, A. Zagrai, and J. Jing Bao, "Piezoelectric wafer embedded active sensors for aging aircraft structural health monitoring," *Structural Health Monitoring,* vol. 1, no. 1, pp. 41-61, 2002, doi: https://doi.org/10.1177/147592170200100104.

[6] V. Giurgiutiu, *Structural health monitoring: with piezoelectric wafer active sensors*. Elsevier, 2007.

[7] L. Pollock and G. Wild, "An initial review of hypersonic vehicle accidents," in *19th Australian International Aerospace Congress*, 2021: Engineers Australia, pp. 111-116, doi: https://search.informit.org/doi/10.3316/informit.313605871683082.

[8] L. Pollock and G. Wild, "Modal Analysis of a Scramjet Inlet for Optimization of Sensor Placement," in *ASCEND 2021*, Las Vegas, Nevada & Virtual, November 15-17, 2021 2021: American Institute of Aeronautics and Astronautics, doi: https://doi.org/10.2514/6.2021-4084.

[9] G. Bartelds, "Aircraft structural health monitoring, prospects for smart solutions from a European viewpoint," *Journal of Intelligent Material Systems and Structures,* vol. 9, no. 11, pp. 906-910, 1998, doi: https://doi.org/10.1177/1045389X9800901106.

[10] T. Dong and N. H. Kim, "Cost-effectiveness of structural health monitoring in fuselage maintenance of the civil aviation industry," *Aerospace,* vol. 5, no. 3, p. 87, 2018, doi: https://doi.org/10.3390/aerospace5030087.

[11] S. S. Kessler, "Certifying a structural health monitoring system: Characterizing durability, reliability and longevity," in *Proceedings of the 1st International Forum on Integrated Systems Health Engineering and Management in Aerospace*, Napa, CA, 2005, pp. 7-10.

[12] S. Findlay and N. Harrison, "Why aircraft fail," *Materials Today,* vol. 5, no. 11, pp. 18-25, 2002, doi: https://doi.org/10.1016/S1369-7021(02)01138-0.

[13] U. G. Goranson, "Fatigue issues in aircraft maintenance and repairs," *International Journal of Fatigue,* vol. 20, no. 6, pp. 413-431, 1998, doi: https://doi.org/10.1016/S0142-1123(97)00029-7.

[14] L. Pollock and G. Wild, "Spectral Domain Analysis of Acousto-Ultrasonic Tone Burst Lamb Wave Emissions in Uncured Pre-Preg Carbon Fiber Composites," in *ASCEND 2021*, Las Vegas, Nevada & Virtual, November 15-17, 2021 2021: American Institute of Aeronautics and Astronautics, doi: https://doi.org/10.2514/6.2021-4233.

[15] J. Gilroy, L. Pollock, and G. Wild, "Fuel and Emission Savings from the use of Lightweight Composite Unit Load Devices," 2022, doi: https://doi.org/10.31224/2270

[16] V. Giurgiutiu, *Structural health monitoring of aerospace composites*. Imprint: Academic Press, 2015.

[17] B. Harris, *Fatigue in composites: science and technology of the fatigue response of fibre-reinforced plastics*. Woodhead Publishing, 2003.

[18] L. Pollock, A. K. Abdelwahab, J. Murray, and G. Wild, "The Need for Aerospace Structural Health Monitoring: A review of aircraft fatigue accidents," *International Journal of Prognostics and Health Management,* vol. 12, 3, 2021, doi: https://doi.org/10.36001/ijphm.2021.v12i3.2368

[19] R. Lammering, U. Gabbert, M. Sinapius, T. Schuster, and P. Wierach, *Lamb-wave based structural health monitoring in polymer composites*. Springer, 2017.

[20] P. Fromme and M. B. Sayir, "Measurement of the scattering of a Lamb wave by a through hole in a plate," *The Journal of the Acoustical Society of America,* vol. 111, no. 3, pp. 1165-1170, 2002, doi: https://doi.org/10.1121/1.1448338.

[21] Y. Kim, S. Ha, and F.-K. Chang, "Time-domain spectral element method for built-in piezoelectric-actuator-induced lamb wave propagation analysis," *AIAA Journal,* vol. 46, no. 3, pp. 591-600, 2008, doi: https://doi.org/10.2514/1.27046.

[22] C. M. Yeum, H. Sohn, and J. B. Ihn, "Lamb wave mode decomposition using concentric ring and circular piezoelectric transducers," *Wave Motion,* vol. 48, no. 4, pp. 358-370, 2011, doi: https://doi.org/10.1016/j.wavemoti.2011.01.001.

[23] M. Werby and H. Überall, "The analysis and interpretation of some special properties of higher order symmetric Lamb waves: The case for plates," *The Journal of the Acoustical Society of America,* vol. 111, no. 6, pp. 2686-2691, 2002, doi: https://doi.org/10.1121/1.1473637.

[24] N. Pei and L. J. Bond, "Higher order acoustoelastic Lamb wave propagation in stressed plates," *The Journal of the Acoustical Society of America,* vol. 140, no. 5, pp. 3834-3843, 2016, doi: https://doi.org/10.1121/1.4967756.

[25] L. Yu and V. Giurgiutiu, "In-situ optimized PWAS phased arrays for Lamb wave structural health monitoring," *Journal of Mechanics of Materials and Structures,* vol. 2, no. 3, pp. 459-487, 2007, doi: https://doi.org/10.2140/jomms.2007.2.459.

[26] M. Moles, N. Dubé, S. Labbé, and E. Ginzel, "Review of ultrasonic phased arrays for pressure vessel and pipeline weld inspections," *Journal of Pressure Vessel Technology,* 2005, doi: https://doi.org/10.1115/1.1991881.

[27] C. Silva, B. Rocha, and A. Suleman, "PZT Network and Phased Array Lamb Wave Based SHM Systems," in *Journal of Physics: Conference Series*, 2011, vol. 305, no. 1: IOP Publishing, p. 012087, doi: https://doi.org/10.1088/1742-6596/305/1/012087.

[28] J. L. Rose, "Successes and challenges in ultrasonic guided waves for NDT and SHM," in *Proceedings of the National Seminar & Exhibition on Non-Destructive Evaluation*, 2009, pp. 10-12.

[29] B. W. Drinkwater and P. D. Wilcox, "Ultrasonic arrays for non-destructive evaluation: A review," *NDT & E International,* vol. 39, no. 7, pp. 525-541, 2006, doi: https://doi.org/10.1016/j.ndteint.2006.03.006.

[30] Y. S. Andhale, F. Masurkar, and N. Yelve, "Localization of Damages in Plain And Riveted Aluminium Specimens using Lamb Waves," *International Journal of Acoustics & Vibration,* vol. 24, no. 1, 2019, doi: https://doi.org/10.20855/ijav.2019.24.11485.

[31] L. Chen, Y. Liu, F. Kong, and N. He, "Acoustic source localization based on generalized cross-correlation time-delay estimation," *Procedia Engineering,* vol. 15, pp. 4912-4919, 2011, doi: https://doi.org/10.1016/j.proeng.2011.08.915.

[32] C. Knapp and G. Carter, "The generalized correlation method for estimation of time delay," *IEEE Transactions on Acoustics, Speech, and Signal Processing,* vol. 24, no. 4, pp. 320-327, 1976, doi: https://doi.org/10.1109/TASSP.1976.1162830.

[33] M. S. Brandstein and H. F. Silverman, "A robust method for speech signal time-delay estimation in reverberant rooms," in *1997 IEEE International Conference on Acoustics, Speech, and Signal Processing*, 1997, vol. 1: IEEE, pp. 375-378, doi: https://doi.org/10.1109/ICASSP.1997.599651.

[34] R. Bracewell, *The Fourier transform and its applications*. McGraw-Hill New York, 1986.

[35] A. Papoulis, "The Fourier integral and its applications," *Physics Today,* 1963, doi: https://doi.org/10.1063/1.3050815.

[36] R. Bracewell, "Pentagram notation for cross correlation. The Fourier transform and its applications," *New York: McGraw-Hill,* vol. 46, p. 243, 1965.

[37] P. R. Roth, "Effective measurements using digital signal analysis," *IEEE Spectrum,* vol. 8, no. 4, pp. 62-70, 1971, doi: https://doi.org/10.1109/MSPEC.1971.5218046.

[38] G. C. Carter, A. H. Nuttall, and P. G. Cable, "The smoothed coherence transform," *Proceedings of the IEEE,* vol. 61, no. 10, pp. 1497-1498, 1973, doi: https://doi.org/10.1109/PROC.1973.9300.

[39] E. L. Ferguson and B. G. Ferguson, "High-precision acoustic localization of dolphin sonar click transmissions using a modified method of passive ranging by wavefront curvature," *The Journal of the Acoustical Society of America,* vol. 146, no. 6, pp. 4790-4801, 2019, doi: https://doi.org/10.1121/1.5138935.

[40] L. Pollock and G. Wild, "Numerical Modelling of Lamb Wave Propagation in 2D Plate Structures," 2023, doi: https://doi.org/10.31224/3009.